Low-Cost Hyperspectral Push-broom Microscope, targeting Smart Farming Applications

Samuel Ortega, Raúl Guerra, Himar Fabelo, María Díaz, Sebastián López, Gustavo Callicó, Roberto Sarmiento
University of Las Palmas de Gran Canaria
Institute of Applied Microelectronic (IUMA), Gran Canaria, Spain
email: sortega@iuma.ulpgc.es

***Abstract*—Currently, the use of hyperspectral imaging (HSI) for the inspection of microscopic samples in an emerging trend in different fields. The use of push-broom hyperspectral (HS) cameras against other HSI technologies is motivated by their high spectral resolution and their capabilities to exploit spectral ranges beyond 1000 nm. Nevertheless, the use of push-broom cameras coupled to microscopes imposes to perform an accurate spatial scanning of the sample to collect the HS data. In this manuscript, we present a methodology to correctly set-up a HS push-broom microscope to acquire high-quality HS images. First, we present a custom 3D printed mechanical system developed to perform the spatial scanning by performing a linear movement that controls the microscope stage. Then, we discuss the most important characteristics of a microscopic HS system and we propose an image analysis method able to quantitatively verify the correct setup of the system prior to acquire high-quality HS images. Finally, we present a set of images acquired from real microscopic samples, showing the potential of HSI for the microscopic analysis.**

***Index Terms*—hyperspectral imaging, microscope, microscopic analysis, push-broom camera**

I. Introduction

In the last decades, hyperspectral imaging (HSI) has become a very popular emerging technique employed in numerous areas and applications. Unlike traditional panchromatic and multispectral (MS) images, hyperspectral (HS) images offer high spectral resolution allowing to collect information of very narrow and continuous spectral bands along the entire electromagnetic spectrum. This HSI characteristic permits to reconstruct the radiance spectrum of every image pixel and consequently, to identify different materials on the basis of their spectral shape. It makes HSI beneficial for many applications such as vegetation and water resource monitoring [1], non-invasive sensing of food-quality [2], geology [3], brain tumor detection [4], diagnosis of multiple cancers [5], [6], [7], among-others.

In general, HSI has been more commonly applied to remote sensing applications. However, the use of HS imagery for microscopic examination of samples has currently attracted the attention of many researchers from different fields [8], such as: mineralogy, for the quantitative analysis of minerals [9]; artworks [10], to identify and classify different pigments; smart farming, to evaluate the disease resistant of plants to different pathogens [11][12]; and medicine, for noninvasive disease diagnosis and surgical guidance [13] [14].

The most widely used methods to acquire the HS images are based on push-broom scanners which generate the HS cube in a line-by-line fashion. This kind of scanners stands as a very competitive alternative which offers high spectral resolution with very reasonable spatial resolution. Furthermore, some regions of the electromagnetic spectrum can only be analysed using this type of HS systems (e.g. from 1100 to 2500 nm). For this reason, HS push-broom systems are adequate to evaluate which spectral range and spectral bands are relevant for a given application. However, their use in HS microscopic applications is very limited due to the higher complexity of ensuring high resolution movements and accurate spatial scanning.

This work is presented as a solution to the limitations imposed by the push-broom scanners to be properly combined with microscopic HS imaging systems. To do this, we present the development of a customized microscope with HS capabilities as well as a general methodology to correctly couple a HS push-broom camera to a microscope to capture high-quality HS images.

II. Instrumentation

In this section, we describe the instrumentation employed in this study, which is composed by two main parts: the optical subsystem (composed by both the microscope optic path and a HS push-broom camera) and the mechanical subsystem, mainly devoted to perform the spatial scanning in the push-broom acquisition system.

A. Optical subsystem

The optical subsystem employed in our system consists of an HS camera coupled to a conventional light microscope. The microscope is an Olympus BH2-MJLT (Olympus, Tokyo, Japan). The main features of this microscope are the dual illumination mode, which allows the observation both in transmittance and reflectance; the trinocular (BH2-TR3), which permits the attachment of a C-mount camera; the objective lenses, which are from the Neo S Plan family (Olympus, Tokyio, Japan) and with five different magnifications: 5x, 10x, 20x, 50x and 100x. The microscope also provides an in-house illumination system based on a 50 W halogen lamp.

The push-broom HS camera is the Hyperspec VNIR A-Series from HeadWall Photonics (Fitchburg, MA, USA), which is based on an imaging spectrometer coupled to a CCD (Charge-Coupled Device) sensor, the Adimec-1000m

(Adimec, Eindhoven, Netherlands). This HS system works in the VNIR (Visual and Near-InfraRed) spectral range from 400 to 1000 nm with a spectral resolution of 2.8 nm, being able to sample 826 spectral channels and 1004 spatial pixels. The HS camera was directly coupled to the microscope using the Olympus MTV-3 C-mount adapter.

The field of view (FOV) captured by the camera will depend both on the lens magnification and the sensor size of the camera, as it can be seen from Equation 1. For this camera, the pixel size is 7.4 μm, while the overall magnification of the optical system is determined by the magnification of each lens. Using this information, we are able to calculate the FOV for the different magnifications. The theoretical FOV is 1.5 mm, 750.45 and 375.23 μm for the $5x$, $10x$ and $20x$ magnifications respectively. As a result, the widths of the push-broom lines are 1.49 μm, 747.46 nm and 373.73 nm.

$$FOV = \frac{Pixel\,Size \cdot Number\,of\,pixels}{Magnification} = \frac{Sensor\,Size}{Magnification} \quad (1)$$

B. Mechanical subsystem

A relative motion between the HS sensor and the targeted sample is needed in order to acquire HS cubes using a push-broom camera. The quality and limitations of the acquired images are strongly related to the characteristics of this relative movement. Due to this reason, a high effort has been made in this work in order to achieve good movement conditions.

In our acquisition system (Fig. 1), the HS sensor remains motionless, placed over the microscope, while the sample to be scanned is moved taking advantage of the microscope moving platform. By default, the movement system of the microscope is a manual one, in which two little handles can be manually rotated for moving the sample in the X and Y directions using two rack and pinion gear mechanisms. A stepper motor was set up for driving the handle corresponding to the X direction. By doing so, the movement in the X direction was turned into an automatic one, which can be controlled from the computer in order to synchronize the sample movement with the sensor acquisition process. The stepper motor is controlled using a DRV8825 driver plugged into an Arduino UNO board, which communicates with the computer through the USB serial port. The stepper motor was mechanically fixed using a custom 3D printed mechanism that includes pulley transmission and a planetary reduction, as it can be seen in Fig. 1. The main goal of this mechanism is to fulfill the mechanical requirements imposed by optical resolution of the optical system.

For the acquisition of HS images in this work, the HS camera is continuously capturing frames, while the sample to be scanned is moving in the X direction according to the motor steps. Two important mechanical restrictions must be fulfilled to acquire high-quality HS images using this kind of scanning. First, the resolution of the mechanical movement system must be considerably higher than the optical resolution, being the mechanical movement of the sample perceived as a continuous and uniform displacement by the scanning

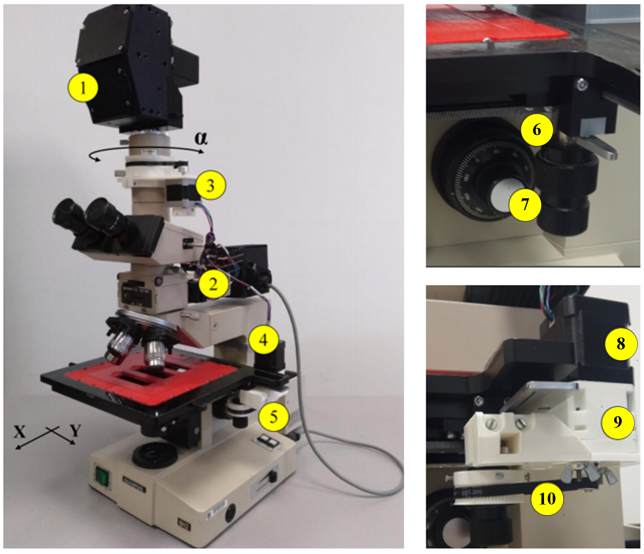

Fig. 1. Acquisition System. 1) VNIR HS camera. 2) Controller of the mechanical system. 3) Camera alignment mechanism. 4) Stepper motor for controlling the sample movement. 5) Custom 3D printed transmission mechanism. 6) Microscope handles for manual movements. 7) Microscope rack and pinion gear mechanism. 8) Stepper motor. 9) Planetary reduction. 10) Pulley reduction.

sensor. On the contrary, there will be gaps between subsequent acquired frames. Secondly, the stepper motor rotation speed has to be neither too high nor too low, so it can efficiently work, avoiding vibrations and overheating. The required motor rotation speed will depend on the mechanical resolution and the linear speed at which the sample has to be moved. This linear speed is determined by the optical resolution and the frame rate at which the sensor is capturing the data.

Generally, the linear movement of the sample is proportional to the movement of the stepper motor, multiplied by the transmission ratio of the system (TR_{system}), as shown in Equations 2 and 3, where D_{linear} refers to the linear distance that the sample is moved for each motor step, and S_{linear} is the linear speed at which the sample is moved according to the rotation speed of the motor, measured in steps per second. $MSPR$ refers to the number of steps per motor revolution.

$$D_{\text{linear}_{(\text{mm/step})}} = TR_{\text{system}_{(\text{mm/rev})}} \cdot \frac{1}{MSPR_{(step/rev)}} \quad (2)$$

$$S_{\text{linear}_{(\text{mm/sec})}} = D_{\text{linear}_{(\text{mm/step})}} \cdot S_{\text{rotation}_{(\text{steps/sec})}} \quad (3)$$

Due to the mechanical requirements for acquisition systems based on push-broom cameras, a mechanical system able to accurately move very short distances and at a very low but continuous and uniform speed is required. Hence, according to Equations 2 and 3, a small TR_{system} value is desired, as well as a high $MSPR$ one. In particular, the selected stepper motor has 400 steps per revolution. Additionally, the DRV8825 driver is able to increase the stepper motor resolution (steps

per revolution) by introducing micro-steps up to a maximum of 32 micro-steps per motor steps. Accordingly, the minimum $MSPR$ for our motor is 400 steps per revolution and the maximum one is 12,800 steps per revolution.

The TR_{system} can be depicted as shown in Equation 4, where $TR_{\text{planetary}}$ refers to the transmission ratio of the planetary reduction placed after the motor, TR_{pulley} refers to the transmission ratio of the pulley reduction placed between the planetary reduction and the microscope handle, and TR_{gear} refers to the transmission ratio of the microscope rack and pinion gear mechanism, measured in millimeters per revolution. The transmission values that corresponds to the custom 3D printed parts are $TR_{\text{planetary}} = 1/5$ and $TR_{\text{pulley}} = 16/64$. The transmission ratio of the rack and pinion gear mechanism is 42 millimeters per revolution (28 teeth with a pitch of 1.5 millimeters). This results in a considerably small transmission ratio ($TR_{\text{system}} = 2.1$ millimeters per revolution). Additionally, more than one planetary reduction can be stacked together for obtaining extra $1/5$ reductions.

$$TR_{\text{system}_{(\text{mm/rev})}} = TR_{\text{planetary}} \cdot TR_{\text{pulley}} \cdot TR_{\text{gear}_{(\text{mm/rev})}} \tag{4}$$

According to these values, the mechanical resolution of the system is 164.0625 nm per motor step. This means that the minimal distance that the sample can be moved is $D_{\text{linear}} = 164.0625$ nm.

C. Calibration instrumentation

In our methodology for setting up a HS/MS push-broom microscope, we employ a microscope calibration slide composed by four different parts: a single axis micrometer scale, a dual axis micrometer scale and two dots with different diameters. The single axis micrometer scale has a length of 10 mm with divisions of 0.1 mm, numbered from 10 to 1. The dual axis scale ranges in 0.01 mm each division, having also additional markers which facilitate measurements of 0.05 mm. Finally, the diameter of the target dots are 0.15 mm and 0.07 mm, respectively.

III. Methodology

In this section, we present a methodology for quantitatively verifying the correct set up of the entire HS microscopic system based on image analysis methods.

A. Empirical assessment of the optical resolution

In this section, we aim to determine the effective FOV measured by the HS camera, which also will reveal the width of the push-broom line. This measure allows to determine the proper scanning speed. For this step, the HS camera should be correctly aligned in order to avoid undesired measurement errors. For the FOV measurement, both the micrometer ruler and the dual axis scale from the calibration slide are employed. Using both calibration targets, it is possible to record images where the distance between lines is known, and hence we can estimate the effective FOV of the camera by performing image analysis over these targets. Fig. 2a represents the push-broom frame from a calibration target, where the distance between lines is known.

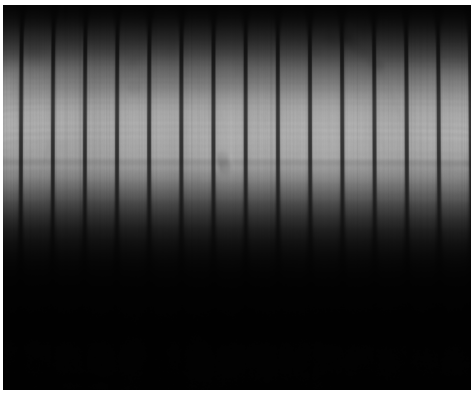

a)

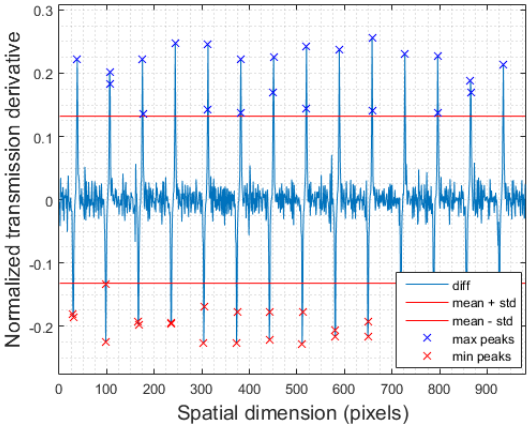

b)

Fig. 2. Micrometer ruler for spatial resolution determination . a) Push-broom frame corresponding to the micrometer scale profile, where the X axis represents the number of pixels of the line and the Y axis represents the spectral bands. b) Distance calculation based on the ruler's profile derivative.

Our image analysis approach has the goal of determining the distance (in pixels) between two consequent lines by finding the edges of the ruler lines, and then counting the pixels between edges in order to estimate the FOV. To this end, we first extract the spatial ruler profile from the push-broom frame. Then, the edges of such frame are identified by calculating the first derivative of the ruler profile. The ruler profile derivative is shown in Fig. 2b, where the positive peaks correspond to the rising edges, and the negative peaks to the falling edges of the ruler profile.

These positive and negative peaks were identified setting a threshold (red line in Fig. 2b) and then, the mean distance (in pixels) between two consecutive peaks of the same sign was estimated. Using this distance, the pixel size and the FOV was calculated.

The estimation of the FOV was carried out for three different magnifications (5x, 10x and 20x), and the micrometer scale allows to measure three different distances (0.1 mm, 0.05 mm and 0.01 mm). Prior to show the experimental estimation

of the FOV for each magnification, some considerations should be highlighted. First, although the calibration slide allows measuring three different distances, the width of the line for 0.05 mm and 0.01 mm divisions keeps constant. For this reason, measures using the 0.01 mm ruler are highly biased by the line width. For an adequate FOV estimation using this methodology, the micrometer ruler should present a low line width compared to the distance between consequent lines. Using this methodology, an agreement between the estimated FOV using Equation 1 and the measured FOV using the ruler profile was found, as we can notice from results collected in Table I.

Distance (mm)	5x (μm)	10x (μm)	20x (μm)
0.1	1,470.62	733.94	366.30
0.05	1,492.58	738.01	368.32
0.01	1,538.53	800.00	392.16
Theoretical	1,500.00	750.46	375.23

TABLE I
MEASURED FOV PER EACH MAGNIFICATION

B. Empirical assessment of the mechanical movement precision and repeatability

As described in Section II-B, the mechanical resolution of the system is a critical characteristic for being able to acquire high-quality HS images. Due to this reason, a stepper motor was set up in the microscope using a custom 3D printed mechanism for automatically controlling the sample movement and theoretically achieving a very high movement resolution ($D_{\text{linear}} = 164.0625$ nm). In on order to verify the precision of the developed mechanism as well as its repeatability and tolerance, the linear displacement of the microscope stage in the X direction when rotating the motor 200,000 steps was measured using a digital caliper gauge. For doing so, the digital caliper gauge was installed also using custom 3D printed parts (Fig. 1). Using this set up a set of 10 measurements were taken. The average distance obtained was 32.94 mm with a standard deviation lower than the 0.3%. According to this value, the minimal distance that the sample could be moved (mechanical resolution) is 164.705 nm. As it can be observed, this value is very closed to the theoretically calculated one ($D_{\text{linear}} = 164.0625$ nm), being the difference lower than the 0.5%.

C. System speed and alignment calibration improvement

The scanning process can produce some morphological deformations in the captured HS images of the samples. For this reason, both the scanning speed and the alignment between the sample and the camera must be correctly configured prior to the acquisition of the HS images. At this stage of the calibration process, the HS camera was aligned by visual inspection. The pixel size was also calculated using the methodology described in Section II-A. Additionally, the spatial resolution of the system was also known (calculated in Section II-B). Using the pixel size, the mechanical resolution and the capturing frame rate of the HS camera (40 ms), the required motor rotation speed can be calculated using Equation 3, as it was described in Section II-B. Hence, HS images with relatively good quality should be obtained using this set up. Nevertheless, one extra stage was carried out in order to improve and/or verify the correct execution of the previous calibration stages. In this calibration stage, the entire acquisition system (microscope, camera and movement mechanism) was considered as a whole. The goal is to capture an image of a circle of the calibration slide and evaluate its spatial appearance in order to determine possible camera misalignment's and/or not optimal movement speeds.

When the image of the calibration slide circle dot is captured at the correct speed, its shape perfectly corresponds with a circle. However, when the speed is too high or too low, its shape seems like an ellipse. Additionally, when the camera is not correctly aligned, the circle seems to be slightly rotated. However, this effect can be better perceived when the speed is too low and the circle seems outstretched. Accordingly, in order to verify the correct alignment of the camera, a low speed was forced in this experiment.

Despite a relatively good assessment of the correct system calibration can be done by visual inspection, an automatic methodology is proposed in order to make it in a more precise and rigorous manner. For such purpose, the circle (or ellipse) eccentricity is used together with a principal component analysis (PCA) method. This automatic methodology is described as follows. First, the image from the circle dot is binarized, generating a single 2D binary image where the pixels corresponding to the circle are labeled as 1 and the background pixels are labeled as 0. Then, a 2D PCA is computed over the binarized circle image. This analysis provides two eigenvalues, corresponding to the directions of the longest and shortest axes of the ellipse ($\lambda_{\max}$ and $\lambda_{\min}$), as well as their corresponding eigenvectors, which conform the rotation matrix, as shown in Fig. 3.

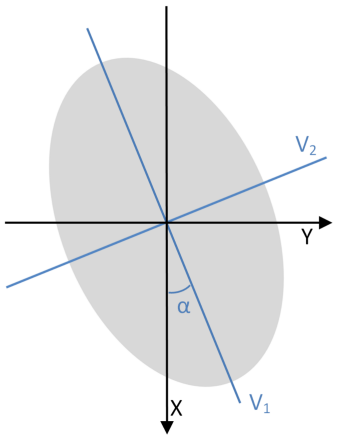

Fig. 3. Principal component analysis of the pixels that conform the ellipse. X represents the sample moving direction. V_1 and V_2 represent the eigenvectors corresponding to the $\lambda_{\max}$ and $\lambda_{\min}$ eigenvalues, respectively. α represents the rotation angle.

The final goal of this methodology is to verify a correct

configuration of both the scanning speed and the camera alignment. Regarding the scanning speed assessment, when capturing a circle using the optimal speed, the obtained eccentricity should be 0. The eccentricity of the ellipse can expressed in terms of its major and minor ($\phi_{\max}$ and $\phi_{\min}$) axes as shown in Equation 5. In order to simplify the calculations, the two eigenvalues extracted in the previous stage are used to calculate the eccentricity, as shown in Equation 5, taking advantage of the fact that $(\phi_{\min})^2/(\phi_{\max})^2 = \lambda_{\min}/\lambda_{\max}$.

$$e = \sqrt{1 - \frac{(\phi_{\min})^2}{(\phi_{\max})^2}} = \sqrt{1 - \frac{\lambda_{\min}}{\lambda_{\max}}} \tag{5}$$

For the assessment of the alignment, the rotation angle calculation based on the PCA analysis was used. Using the first eigenvector of the rotation matrix, V_1, which corresponds to the first eigenvalue, the "counterclockwise" rotation angle, with respect to the X axis, α, was calculated as shown in Equation 6. For simplicity, we considered the first eigenvalue as the largest one, and hence, the rotation angle can be represented as shown in Fig. 3. This angle is equivalent to the camera misalignment. If the obtained angle value is 0 or 90 it means that the HS camera is perfectly aligned. Notice that for making this calculation it is better to set a relatively low speed in order to obtain an outstretched appearance of the ellipse, being 0 the desirable angle value. If a relatively high speed were used, the desirable angle value would be 90. It is also important to highlight that the axis are rotated 90 clockwise so that the X axis of the captured image corresponds with the sample moving direction (X).

$$\alpha = \arctan(\frac{V_{1_y}}{V_{1_x}}) \tag{6}$$

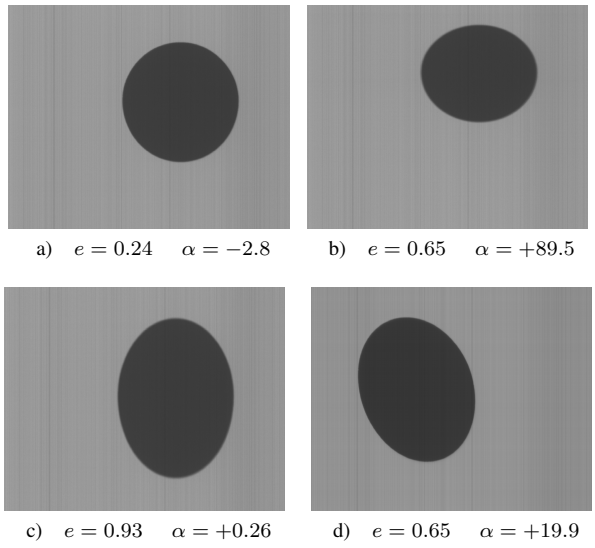

Fig. 4. Real examples of the results provided by the described methodology. a-c) Examples of different scanning speed configurations (camera aligned). d) Example of misalignment between the camera and the microscope (bad scanning speed configuration)

Fig. 4 displays a set of example HS images of the black dot sample collected by the system, as well as the alignment and eccentricity values provided by the described method. First, the influence of the mechanical scanning speed in the captured images is shown in Fig. 4a to 4c. For such images, the HS camera and the microscope were correctly aligned prior to acquisition. Fig. 4a presents the situation of an image captured using the optimal scanning speed, while Fig. 4b and Fig. 4c show images acquired with lower or faster speed, respectively. In this example we show how the eccentricity can be used as an indicator of a correct speed scanning. Furthermore, Figure 4d displays an scenario where a misalignment between the HS camera and the microscope was forced. To highlight the misalignment, this image was captured using a low scanning speed. In this results it is possible to observe how the rotation angle of the described methodology can be used to ensure the correct alignment of the system.

IV. Experiments and Results

The preliminary results obtained with the developed HS microscopic system are presented in Fig.5, where the synthetic RGB representations of the HS cubes obtained from a microscopic slide sample at different magnifications are presented. The specimens under evaluation are prepared slides from Brunel Microscopes (Brunel Microscopes, Wiltshire, U.K.), Specifically, a pine stem sample (*BS17 Stem Structure*) was captured.

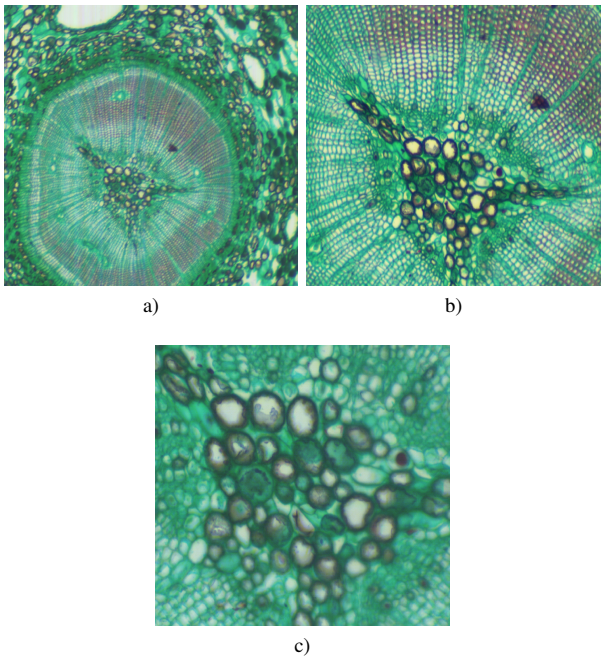

Fig. 5. RGB representation of the H data collected using different magnifications for the pine stem sample using different magnifications. a) 5x. b) 10x, c) 20x

For the 20x magnification images, where the smallest details of the stem sample are able to be observed, we select a few amount of pixels from the HS cube and we represented the

spectral signatures of such pixels. Such spectral signatures are shown in 6, where different parts of the Pine Stem present different spectral signatures.

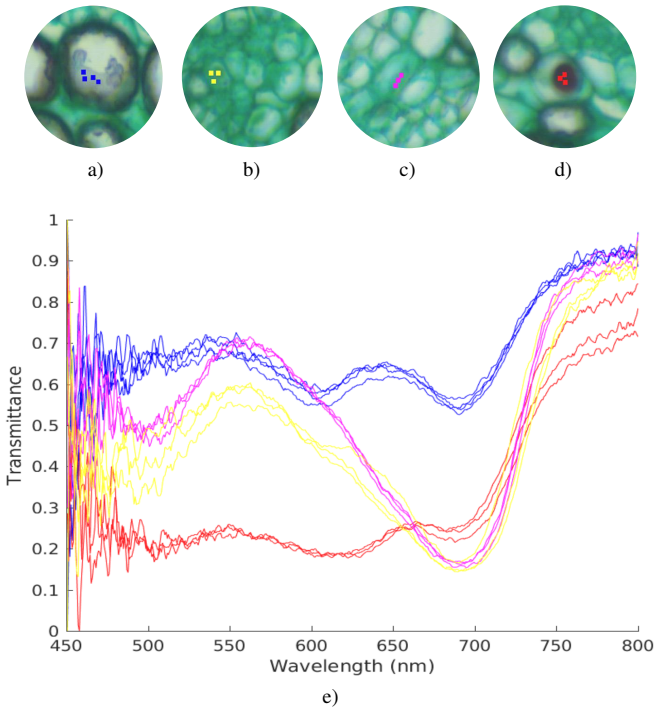

Fig. 6. Spectral signatures present in the pine stem sample.(a-d) Regions of interest where we select some pixels in different colors from the 20x sample. e) Spectral signatures corresponding to the pixels highlighted in (a-d).

V. Conclusion

In this research we present a custom low-cost mechanism able to be attached to a conventional microscope in order to perform the spatial scanning required by HS push-broom cameras. In addition, we propose an image analysis method to retrieve information from any microscopic HS system based on a push-broom camera and also a methodology to verify that both the speed and the alignment are correct, ensuring images presenting no morphological distortions. Finally, we show some examples of HS images from a pine stem, showing differences between the spectral signatures of the different components of the image. This work is intended to provide a general framework to configure the parameters of a push-broom HS based microscope for acquiring high-quality images. Future works related to the instrumentation will be focused in using this methodology to compare our custom scanning system with a commercial one. Nevertheless, the work presented herein is the first stage on the capture process of samples for smart farming applications, such as the detection of diseased plants.

Acknowledgment

This work has been supported in part by the Canary Islands Government through the ACIISI (Canarian Agency for Research, Innovation and the Information Society), ITHACA project "Hyperspectral Identification of Brain Tumours" under Grant Agreement ProID2017010164 and the Ministry of Economy and Competitiveness (MINECO) of the Spanish Government (PLATINO project, no. TEC2017-86722-C4-1-R). This work was completed while both Samuel Ortega and María Díaz were beneficiaries of a pre-doctoral grant given by the "Agencia Canaria de Investigación, Innovación y Sociedad de la Información (ACIISI)" of the "Conserjería de Economía, Industria, Comercio y Conocimiento" of the "Gobierno de Canaria", which is part-financed by the European Social Fund (FSE) (POC 2014-2020, Eje 3 Tema Prioritario 74 (85%))

References

[1] M. Govender, K. Chetty, and H. Bulcock, "A review of hyperspectral remote sensing and its application in vegetation and water resource studies," *Water Sa*, vol. 33, no. 2, 2007.

[2] G. M. ElMasry and S. Nakauchi, "Image analysis operations applied to hyperspectral images for non-invasive sensing of food quality–a comprehensive review," *Biosystems engineering*, vol. 142, pp. 53–82, 2016.

[3] F. D. Van der Meer, H. M. Van der Werff, F. J. Van Ruitenbeek, C. A. Hecker, W. H. Bakker, M. F. Noomen, M. Van Der Meijde, E. J. M. Carranza, J. B. De Smeth, and T. Woldai, "Multi-and hyperspectral geologic remote sensing: A review," *International Journal of Applied Earth Observation and Geoinformation*, vol. 14, no. 1, pp. 112–128, 2012.

[4] S. Ortega, H. Fabelo, R. Camacho, M. de la Luz Plaza, G. M. Callicó, and R. Sarmiento, "Detecting brain tumor in pathological slides using hyperspectral imaging," *Biomedical Optics Express*, vol. 9, no. 2, p. 818, feb 2018. [Online]. Available: https://www.osapublishing.org/abstract.cfm?URI=boe-9-2-818

[5] D. G. Ferris, R. A. Lawhead, E. D. Dickman, N. Holtzapple, J. A. Miller, S. Grogan, S. Bambot, A. Agrawal, and M. L. Faupel, "Multimodal hyperspectral imaging for the noninvasive diagnosis of cervical neoplasia," *Journal of Lower Genital Tract Disease*, vol. 5, no. 2, pp. 65–72, 2001.

[6] H. Akbari, L. Halig, D. M. Schuster, B. Fei, A. Osunkoya, V. Master, P. Nieh, and G. Chen, "Hyperspectral imaging and quantitative analysis for prostate cancer detection," *Journal of biomedical optics*, vol. 17, no. 7, p. 076005, 2012.

[7] A. O. N. Joseph, *Hyperspectral optical imaging for detection, diagnosis and staging of cancer*. University of Southern California, 2012.

[8] R. A. Schultz, T. Nielsen, J. R. Zavaleta, R. Ruch, R. Wyatt, and H. R. Garner, "Hyperspectral imaging: a novel approach for microscopic analysis," *Cytometry*, vol. 43, no. 4, pp. 239–247, 2001.

[9] E. Pirard, "Multispectral imaging of ore minerals in optical microscopy," *Mineralogical Magazine*, vol. 68, no. 02, pp. 323–333, apr 2004.

[10] J. van der Weerd, M. K. van Veen, R. M. Heeren, and J. J. Boon, "Identification of pigments in paint cross sections by reflection visible light imaging microspectroscopy," *Analytical Chemistry*, vol. 75, no. 4, pp. 716–722, 2003.

[11] A.-K. Mahlein, "Plant Disease Detection by Imaging Sensors Parallels and Specific Demands for Precision Agriculture and Plant Phenotyping," *Plant Disease*, vol. 100, no. 2, pp. 241–251, feb 2016. [Online]. Available: http://apsjournals.apsnet.org/doi/10.1094/PDIS-03-15-0340-FE

[12] M. Leucker, A.-K. Mahlein, U. Steiner, and E.-C. Oerke, "Improvement of Lesion Phenotyping in Cercospora beticola Sugar Beet Interaction by Hyperspectral Imaging," *Phytopathology*, vol. 106, no. 2, pp. 177–184, feb 2016. [Online]. Available: http://apsjournals.apsnet.org/doi/10.1094/PHYTO-04-15-0100-R

[13] B. S. Sorg, B. J. Moeller, O. Donovan, Y. Cao, and M. W. Dewhirst, "Hyperspectral imaging of hemoglobin saturation in tumor microvasculature and tumor hypoxia development," *Journal of biomedical optics*, vol. 10, no. 4, p. 044004, 2005.

[14] A. M. Siddiqi, H. Li, F. Faruque, W. Williams, K. Lai, M. Hughson, S. Bigler, J. Beach, and W. Johnson, "Use of hyperspectral imaging to distinguish normal, precancerous, and cancerous cells," *Cancer Cytopathology: Interdisciplinary International Journal of the American Cancer Society*, vol. 114, no. 1, pp. 13–21, 2008.